Experimental and numerical investigation of S700 high strength steel CHS beam-columns after exposure to fire

Yukai Zhong [a], Ou Zhao [a,*], Leroy Gardner [b]

[a] School of Civil and Environmental Engineering, Nanyang Technological University, Singapore

[b] Department of Civil and Environmental Engineering, Imperial College London, UK

[*] Corresponding author, Email: ou.zhao@ntu.edu.sg

Abstract

This paper presents an experimental and numerical investigation into the post-fire behaviour and residual capacity of S700 high strength steel circular hollow section (CHS) beam-columns. The experimental investigation was performed on ten S700 high strength steel CHS beam-columns and included heating and cooling of the specimens as well as post-fire material testing, initial global geometric imperfection measurements and pin-ended eccentric compression tests. A subsequent numerical investigation was conducted, where finite element models were developed and validated against the test results and then employed to carry out parametric studies to generate further numerical data over a wide range of cross-section dimensions, member lengths and loading combinations. In view of the fact that there are no specific provisions for the design of steel structures after exposure to fire, the relevant room temperature design interaction curves were evaluated, using post-fire material properties, to assess their applicability to S700 high strength steel CHS beam-columns after exposure to fire, based on the test and numerical data. The evaluation results revealed that the interaction curves provided in the American Specification and Australian Standard result in a high level of design accuracy and consistency, while the Eurocode interaction curve leads to more conservative and scattered failure load predictions. Finally, a revised Eurocode interaction curve, with more accurate end points, was proposed and shown to offer improved failure load predictions for S700 high strength steel CHS beam-columns after exposure to fire.

Keywords: Beam-column tests; CHS beam-columns; Design analysis; Design interaction curve; Heating and cooling; Numerical modelling, Post-fire residual capacity, S700 high strength steel

1. Introduction

High strength steels have superior high strength-to-weight ratios relative to conventional normal strength steels, facilitating the design and construction of lighter, taller and longer span structures. Research on high strength steel structures in fire and post-fire scenarios has been conducted, with the key experimental and numerical studies introduced herein. Qiang et al. [1, 2], Xiong and Liew [3], Li and Young [4] and Ban et al. [5] conducted a series of steady and transient state tests on different grades of high strength steel and investigated their mechanical properties and stress–strain curves at elevated temperatures. On the basis of the steady and transient state test results, stiffness and strength reduction factors were determined and new predictive models were developed. The thermal properties of high strength steels at elevated temperatures, including the thermal expansion, specific heat and thermal conductivity, were experimentally studied by Xing et al. [6], with new predictive formulae proposed. The post-fire residual material properties of high strength steels with yield stresses ranging from 460 MPa to 1200 MPa have been studied in a series of testing programmes [7–17]. The test results revealed that the extent of reduction in material properties of high strength steels after exposure to fire is different to that of normal strength steels, and new formulae were developed for predicting the post-fire residual material properties of high strength steels. Moreover, the influence of cooling methods, including cooling in air, water, fire-fighting foam and liquid nitrogen, on the post-fire residual material properties of high strength steels [12, 14–16] were investigated and quantified. Su et al. [13] measured the membrane residual stresses in S690 high strength steel welded I-sections after exposure to elevated temperatures ranging from 30 °C to 950 °C, studied their distributions and magnitudes, and proposed predictive models. Wang et al. [18, 19] and Sharhan et al. [20] conducted steady and transient state tests on Q460, Q690 and Q960 high strength steel welded I-section stub columns at elevated temperatures, investigated their local buckling behaviour, quantified the reductions in load-carrying capacities and evaluated the relevant design provisions. The post-fire cross-sectional behaviour and residual compression resistances of S690 high strength steel welded I-section stub columns were investigated by Su et al. [21] through testing and numerical modelling; on the basis of the test and numerical data, the room temperature slenderness limits were assessed in conjunction with the post-fire material properties for their applicability to the cross-section classification of S690 high strength steel welded I-section stub columns after exposure to elevated temperatures. The global buckling behaviour of S460 high strength steel welded I-section columns in fire was experimentally and numerically studied by Wang et al. [22], with the key influencing factors, including the applied load ratio, axial and rotational restraints and member slenderness ratio, evaluated and verified. Wang and Liu [23] and Li et al. [24] conducted experimental and numerical investigations into the flexural buckling behaviour of high strength steel box and I-section columns after exposure to fire and proposed design methods to predict their residual compression capacities. Complementing the existing research on the fire and post-fire performance of high strength steel structures, as well as the studies into the room temperature response of high strength steel circular hollow section (CHS) beam-columns [25, 26], the present study focuses on the global buckling behaviour of S700 high strength steel CHS beam-columns after exposure to fire.

In the present paper, a testing programme on ten S700 high strength steel CHS beam-columns after exposure to different levels of elevated temperature up to 1100 °C is firstly described. The post-fire beam-column test results are then used in a numerical modelling programme to validate finite element models, based on which, parametric studies are presented, where the test data bank is expanded over a wider range of cross-section dimensions, member lengths and loading combinations. On the basis of the experimentally and numerically obtained data, the relevant room temperature design interaction curves, as provided in ANSI/AISC 360-16 [27], AS 4100 [28] and EN 1993-1-12 [29], are then assessed, using post-fire material properties, for their applicability to S700 high strength steel CHS beam-columns after exposure to elevated temperatures. Finally, a new design interaction curve is proposed.

2. Testing programme

2.1 Test specimens

A testing programme was firstly performed to generate a test data pool on S700 high strength steel CHS beam-columns after exposure to elevated temperatures. Two sizes of CHS – CHS 139.7 × 10 and CHS 168.3 × 4, which were cold-rolled and seam-welded from S700 MC high strength steel sheets, were adopted in the present testing programme. Note that the adopted CHS 139.7 × 10 and CHS 168.3 × 4 are respectively defined as Class 1 and Class 4 at room temperature, according to the slenderness limits in EN 1993-1-12 [29]. For each CHS, five geometrically nominally identical beam-column specimens were examined; four were exposed to different nominal elevated temperatures – T=400 °C, 600 °C, 900 °C and 1100 °C, while the fifth specimen remained unheated. All five specimens were then tested at room temperature under eccentric compression loads with the same nominal initial loading eccentricity. Table 1 reports the measured values of the key geometric parameters for each specimen, including the cross-section outer diameter D and wall thickness t as well as the member length L. The specimen ID comprises the cross-section identifier 'D140' or 'D168' (with 'D140' signifying the CHS 139.7 ×10 and 'D168' representing the CHS 168.3 ×4), a letter 'T' along with the nominal target exposure temperature (e.g., 'T600' standing for the nominal target exposure temperature of 600 °C) and a letter 'E' along with the nominal initial loading eccentricity (e.g., 'E50' indicating the nominal initial loading eccentricity of 50 mm).

2.2 Heating and cooling

The S700 high strength steel CHS beam-column specimens, together with tensile coupons extracted from the same batch of tubes, were heated in an electric furnace. The furnace contained a total of eighteen heating elements uniformly distributed along the two longer sides of the chamber, as shown in Fig. 1, to provide even and stable elevated temperatures throughout the chamber during the heating process. An embedded temperature probe was used to monitor the air temperature in the chamber, while five type-K thermocouples, attached to the specimens at different positions, were used to measure their surface temperatures. The heating rate was set as 10 °C/min, which lies within the range of heating rates typically experienced by protected steel structures in fire [30–33]. Upon reaching the target temperature, the temperature was held constant for a soaking period of 30 min, to ensure a stable and uniform temperature distribution within the specimens. Once the heating and soaking processes had been completed, the electric furnace was turned off and all the specimens cooled down naturally to room temperature. The temperature–time histories measured from the five type-K thermocouples for a typical set of S700 high strength steel CHS beam-column and coupon specimens are shown in Fig. 2. Table 2 reports the average measured peak temperature T_m from the five type-K thermocouples for each set of specimens. As depicted in Fig. 3, the surface colours of S700 high strength steel became increasingly dark as the exposure temperatures increase; more specifically, the surface colours turned to dark grey, light brown, light cyan and deep cyan for the exposure temperatures of 400 °C, 600 °C, 900 °C and 1100 °C, respectively. The change of surface colour results from the fact that oxide layers of different thicknesses form at different elevated temperatures during heating [13, 34, 35] and later reflect light of different wavelengths at room temperature.

2.3 Material testing

Upon completion of the heating and cooling processes, the coupons were tested in tension in a Schenck 250 kN servo-hydraulic testing machine, to obtain their post-fire material properties. The instrumentation adopted for the tensile coupon tests is shown in Fig. 4, including an extensometer mounted over the central 50 mm of the coupons to measure the elongations and two strain gauges adhered at the mid-height of the coupons to measure the strains. The measured stress–strain curves of the coupons extracted from the CHS 139.7 × 10 and CHS 168.3 × 4 profiles are shown in Figs 5(a) and 5(b), respectively. Table 2 reports the measured values of the key material parameters, including the Young's modulus E, the yield stress f_y, the ultimate stress f_u, the strain at the ultimate stress ε_u and the fracture strain ε_f; note that the yield stress was taken as the lower bound of the yield plateau for the coupons with clearly-defined yield plateaus but the 0.2% proof stress for the coupons without yield plateaus. On the basis of the results presented in Fig. 5 and Table 2, it is evident that (i) the Young's modulus of S700 high strength steel after exposure to elevated temperatures generally remains unchanged, (ii) the yield and ultimate stresses increase slightly for exposure temperatures up to 600 °C but reduce rapidly for higher exposure temperatures, and (iii) the ultimate and fracture strains show an increasing trend, as the exposure temperatures increase.

2.4 Initial global geometric imperfection measurements

Initial global geometric imperfections influence the buckling behaviour and resistances of steel structural elements [23–26, 33, 36, 37]. Initial global geometric imperfection measurements were therefore performed on the ten S700 high strength steel CHS beam-column specimens after exposure to elevated temperatures. The measurement setup is shown in Fig. 6, where an LVDT is moved longitudinally along the uppermost edge of a specimen, with the displacement readings recorded at the mid-height and near the two ends (50 mm away from each end, for the purpose of eliminating the effect of end flaring [38]). The magnitude of the initial mid-height global geometric imperfection was defined as the deviation from the data point measured at the mid-height to a reference line connecting the data points measured near the two ends. Upon completion of the first measurement, the specimen was rotated by 60° about the longitudinal axis and the measurement procedure was repeated until the initial mid-height global geometric imperfection magnitudes had been obtained for all six radial directions [33], as shown in Fig. 6. The largest value measured in all the six radial directions was finally taken as the initial global geometric imperfection magnitude of the specimen ω_g, as reported in Table 1.

2.5 Beam-column tests

After being exposed to the different levels of elevated temperature, the S700 high strength steel CHS beam-column specimens were tested under eccentric compression, to investigate their post-fire buckling behaviour and residual capacity under combined compression and bending.

A displacement-controlled Instron 5000 kN servo-hydraulic testing machine, driven at a rate of 0.4 mm/min, was used for conducting all the eccentric compression tests. A knife-edge device, consisting of a wedge plate (containing a knife-edge wedge) and a pit plate (containing a semi-circular groove) – see Fig. 7, was positioned at each end of the testing machine, to provide pin-ended boundary conditions. Before testing, each specimen was welded with end plates and placed between the top and bottom wedge plates, with its position adjusted to ensure that (i) the longitudinal axis of the specimen was perpendicular to the wedge plates, (ii) the radial direction resulting in the maximum magnitude of the initial global geometric imperfection intersected with the knife edge at right angles and (iii) the distance from the knife edge to the centroid of the specimen end section was approximately equal to the target initial loading eccentricity. Upon completion of the member alignment and position adjustment, the specimen was secured at both ends through bolting the welded end plates to the wedge plates. It is worth noting that the distance from the specimen end to the corresponding centre of rotation of the knife-edge device is 70 mm (see Fig. 7) and the effective member length of each specimen is thus taken as L_e=L+140 mm.

Fig. 7 displays the beam-column test setup, where the apparatus and instrumentation include a horizontally-orientated LVDT at the mid-height of the specimen to measure the lateral deflections and two strain gauges adhered to the extreme fibres of the specimen at mid-height to record the corresponding strains along the longitudinal direction. The readings from the LVDT and strain gauges were used for calculating the actual initial loading eccentricity e_0, according to Eq. (1) [37, 39, 40], where I is the second moment of area, ε_{max}–ε_{min} is the difference in longitudinal strain measured from the two strain gauges, N is the applied eccentric compression load and Δ is the mid-height lateral deflection measured from the LVDT. It is worth highlighting that the derivation of Eq. (1) is based on the assumption of linear elastic structural behaviour and that the eccentric compression loads N used in the calculation of e_0 were limited to 15% of the failure load [39, 40].

$$e_0 = \frac{EI(\varepsilon_{max} - \varepsilon_{min})}{DN} - \Delta - \omega_g \quad (1)$$

The key obtained experimental results for each S700 high strength steel CHS beam-column specimen are reported in Table 3, including the (calculated) actual initial loading eccentricity e_0, the failure load N_u, the mid-height lateral deflection corresponding to the failure load Δ_u and the first-order elastic moment at the failure load $M_{u,1st,el}$, the second-order elastic moment at the failure load $M_{u,2nd,el}$ and the second-order inelastic moment at the failure load $M_{u,2nd,inel}$, which were determined from Eqs (2)–(4), respectively [39, 41].

$$M_{u,1st,el} = N_u\left(e_0 + \omega_g\right) \quad (2)$$

$$M_{u,2nd,el} = \frac{N_u\left(e_0 + \omega_g\right)}{1 - \dfrac{N_u L_e^2}{\pi^2 EI}} \quad (3)$$

$$M_{u,2nd,inel} = N_u\left(e_0 + \omega_g + \Delta_u\right) \quad (4)$$

The load–mid-height lateral deflection curves measured for the CHS 139.7 × 10 and CHS 168.3 × 4 beam-column specimens are displayed in Figs 8(a) and 8(b), respectively. The failure mode of all the CHS 139.7 × 10 beam-column specimens was global buckling, as shown in Fig. 9(a), while that of the CHS 168.3 × 4 beam-column specimens featured local–global interactive buckling, as displayed in Fig. 9(b).

3. Numerical modelling

3.1 General

A supplementary numerical modelling programme was conducted using the general-purpose finite element (FE) analysis software ABAQUS [42]. FE models were firstly developed and validated against the experimental results. Upon validation, the FE models were employed to carry out parametric studies to generate further numerical data on S700 high strength steel CHS beam-columns after exposure to elevated temperatures over a wide range of cross-section dimensions, member lengths and loading combinations.

3.2 Development of FE models

Each S700 high strength steel CHS beam-column FE model was developed according to the measured cross-section dimensions and effective member length. The shell element S4R [42], which has been extensively employed for modelling high strength steel tubular sections [25, 26, 36, 37, 43, 44], was used herein. On the basis of a prior mesh sensitivity study considering mesh sizes from $0.01D \times 0.01D$ to $0.1D \times 0.1D$, the final mesh size was selected as $0.05D \times 0.05D$, which led to a good balance between computational accuracy and efficiency. With regard to the material modelling, a multi-linear elastic-plastic stress–strain model with the von

Mises yield criterion and isotropic hardening [42] was adopted and required the (measured) engineering stress–strain curves to be converted into the true stress–plastic strain curves. For ease of application of boundary conditions, each end section of the modelled S700 high strength steel CHS beam-columns was firstly coupled to an eccentric reference point, with the eccentricity equal to the corresponding calculated value e_0 (see Table 3). Then, the boundary conditions were assigned to the reference points; more specifically, the top reference point was allowed to rotate about the buckling axis as well as to translate along the member longitudinal axis, while the bottom reference point was only free to rotate about the same buckling axis but held in position, for the purpose of replicating the experimental pin-ended boundary conditions. Initial global and local geometric imperfections were incorporated into each modelled S700 high strength steel CHS beam-column, with the respective distribution profiles assumed to be the lowest elastic global and local buckling mode shapes, as derived from eigenvalue buckling analyses [25, 26, 36, 37, 43]. Three global imperfection magnitudes, including the measured value ω_g and two generalised values, $L_e/1000$ and $L_e/1500$, in combination with two local imperfection magnitudes, both generalised values, $t/10$ and $t/100$, were used to factor the corresponding distribution profiles; this led to a total of six combinations of global and local imperfection magnitudes being examined.

3.3 Validation study

The developed S700 high strength steel CHS beam-column FE models were solved by means of static Riks analyses [42], to obtain the failure loads, full load–deformation histories and failure modes. The obtained numerical results were then compared with the corresponding test results, to evaluate the accuracy of the developed FE models. The FE to test failure load ratios for the ten S700 high strength steel CHS beam-column specimens are reported in Table 4, revealing that (i) the FE failure loads are influenced by both the global and local imperfection magnitudes, (ii) all the six imperfection magnitude combinations lead to relatively accurate predictions of the test failure loads, (iii) the best agreement between the test and FE failure loads is achieved when the measured global imperfection magnitude ω_g, combined with the generalised local imperfection magnitude $t/100$, is employed, and (iv) the test failure loads are also well predicted using the imperfection magnitude combination of $L_e/1000$ and $t/100$. The test and FE load–deformation histories for all the S700 high strength steel CHS beam-column specimens are compared in Fig 10, with the results showing that the test load–mid-height lateral deflection curves can accurately be simulated. Moreover, the test global and local–global interactive buckling failure modes for typical S700 high strength steel CHS beam-column specimens D140-T600-E50 and D168-T600-E50 are also accurately replicated by their FE counterparts, as illustrated in Figs 11(a) and 11(b). In summary, the test structural responses of the S700 high strength steel CHS beam-column specimens after exposure to elevated temperatures can be simulated by the developed FE models, which are therefore regarded as having been validated.

3.4 Parametric studies

Parametric studies were carried out by utilising the validated FE models, to generate a numerical data bank on S700 high strength steel CHS beam-columns after exposure to elevated temperatures over a wide range of cross-section dimensions, member lengths and loading combinations. Specifically, the outer diameters of the modelled CHS were kept constant at 100 mm and a series of wall thicknesses between 1.07 mm and 11.30 mm were chosen, with the resulting $D/(t\varepsilon^2)$ ratios at room temperature ranging from 30 to 100 to cover all four classes of CHS specified in EN 1993-1-12 [29], where $\varepsilon = \sqrt{235/f_y}$. The member lengths were varied to result in member non-dimensional slendernesses from 0.2 to 2.0 being investigated. The initial loading eccentricities ranged from 5 mm to 600 mm, to provide an extensive set of combinations of compression load and bending moment. For each modelled S700 high strength steel CHS beam-column, the initial global and local geometric imperfection magnitudes were respectively taken as $L_e/1000$ and $t/100$ and the measured material properties of the CHS 168.3×4 at room temperature and after exposure to elevated temperatures were assigned. Overall, a total of 560 parametric study results have been generated.

4. Design analyses

4.1 General

Owing to the lack of specific design rules for steel structures after exposure to fire, the relevant room temperature design interaction curves, as provided in ANSI/AISC 360-16 [27], AS 4100 [28] and EN 1993-1-12 [29], were evaluated, using post-fire material properties, for their applicability to S700 high strength steel CHS beam-columns after exposure to fire. For each code, the failure loads $N_{u,pred}$ were firstly predicted according to the room temperature design interaction curve combined with post-fire material properties, and then compared with the test and FE failure loads N_u. Note that all partial safety factors have been set equal to unity in the design calculations, allowing the unfactored failure load predictions to be evaluated. Table 5 presents the results of the quantitative evaluations for each code, including the mean ratio of $N_u/N_{u,pred}$ and the coefficient of variation (COV), arranged by exposure temperature. Graphical comparisons are displayed in Figs 13–15, where the $N_u/N_{u,pred}$ ratio is plotted against the angle θ. The angle $\theta = \tan^{-1}[(N_{u,pred} / N_R) / (M_{u,pred} / M_R)]$ is a parameter used to reflect the combination of compression and bending [39], as illustrated in Fig. 12, where M_R and N_R are the cross-section bending resistance and column flexural buckling resistance, respectively, while $M_{u,pred}=N_{u,pred}e_0$ is the design failure moment; note that θ=0° and θ=90° represent the isolated loading cases of pure bending and pure compression, respectively, while 0°<θ<90° correspond to combined loading cases. A revised Eurocode design interaction curve is also proposed.

4.2 ANSI/AISC 360-16 (AISC)

The current American specification ANSI/AISC 360-16 [27] employs a two-stage interaction curve for the design of CHS beam-columns under combined compression and bending at room temperature, as expressed by Eq. (5),

$$\begin{cases} \dfrac{N_{u,pred}}{N_c} + \dfrac{8}{9}\dfrac{M_{u,pred}}{\alpha_{AISC} M_c} \le 1 & \text{for } \dfrac{N_{u,pred}}{N_c} \ge 0.2 \\ \dfrac{N_{u,pred}}{2N_c} + \dfrac{M_{u,pred}}{\alpha_{AISC} M_c} \le 1 & \text{for } \dfrac{N_{u,pred}}{N_c} < 0.2 \end{cases} \tag{5}$$

where N_c is the AISC column flexural buckling resistance, as calculated in accordance with the critical stress method specified in Clause E3, M_c is the AISC cross-section bending resistance, which is dependent on the cross-section type and given by Eq. (6), where W_{pl} and W_{el} are the plastic and elastic section moduli, respectively, and $\alpha_{AISC} = 1 - N_{u,pred} / N_{cr}$ is the amplification factor to consider second-order effects, where $N_{cr} = \pi^2 EI / L_e^2$ is the Euler critical load. It is worth noting that N_c and M_c are the compression and bending end points of the AISC design interaction curve, while α_{AISC} and other constant factors in Eq. (5) define the shape of the curve.

$$M_c = \begin{cases} W_{pl} f_y & \text{for compact CHS} \\ W_{el}\left(\dfrac{0.021E}{D/t} + f_y\right) & \text{for non-compact CHS} \\ W_{el}\left(\dfrac{0.33E}{D/t}\right) & \text{for slender CHS} \end{cases} \tag{6}$$

The AISC design interaction curve was assessed for its applicability to S700 high strength steel CHS beam-columns after exposure to elevated temperatures. The mean ratios of test and FE to predicted failure loads and the corresponding COVs are reported in Table 5, while the test and FE to predicted failure load ratios $N_u/N_{u,pred}$ are plotted against θ in Fig. 13. On the basis of both the quantitative and graphical assessment results, it can be concluded that the AISC design interaction curve results in overall accurate and consistent failure load predictions when applied to S700 high strength steel CHS beam-columns after exposure to elevated temperatures.

4.3 AS 4100 (AS)

The design interaction curve for CHS beam-columns subjected to combined compression and bending at room temperature, as specified in the current Australian standard AS 4100 [28], is given by Eq. (7), where N_s is the AS column flexural buckling resistance, determined as the product of the cross-section compression resistance and a buckling reduction factor, M_s is the AS cross-section bending resistance calculated based on an effective section modulus method, and $\alpha_{AS} = 1 - N_{u,pred} / N_{cr}$.

$$\frac{N_{u,pred}}{N_s} + \frac{M_{u,pred}}{\alpha_{AS} M_s} \leq 1 \tag{7}$$

The applicability of the AS design interaction curve to S700 high strength steel CHS beam-columns after exposure to elevated temperatures was evaluated. Quantitative and graphical evaluations are presented in Table 5 and Fig. 14, respectively, with the results revealing that the AS design interaction curve leads to an overall good level of accuracy and consistency in predicting the post-fire failure loads for S700 high strength steel CHS beam-columns, though the predictions are slightly more conservative and scattered than their AISC counterparts.

4.4 EN 1993-1-12 (EC3)

With regard to the design of CHS beam-columns at room temperature, the interaction curve provided in EN 1993-1-12 [29] is defined by Eq. (8),

$$\frac{N_{u,pred}}{N_{b,Rd}} + k\frac{M_{u,pred}}{M_{Rd}} \leq 1 \tag{8}$$

where $N_{b,Rd}$ is the EC3 column flexural buckling resistance calculated based on the EC3 buckling curve 'c' with the imperfection factor α taken as 0.49, M_{Rd} is the EC3 cross-section bending resistance given by Eq. (9), and k is the interaction factor, which is defined by Eq. (10) for Class 1 and 2 CHS but Eq. (11) for Class 3 and 4 CHS, where $n = N_{u,pred} / N_{b,Rd}$ is the compression load ratio and $\bar{\lambda}$ is the member non-dimensional slenderness.

$$M_{Rd} = \begin{cases} W_{pl} f_y & \text{for Class 1 and 2 CHS} \\ W_{el} f_y & \text{for Class 3 CHS} \\ W_{eff} f_y & \text{for Class 4 CHS} \end{cases} \tag{9}$$

$$k = \begin{cases} 1 + (\bar{\lambda} - 0.2)n & \text{for } \bar{\lambda} < 1.0 \\ 1 + 0.8n & \text{for } \bar{\lambda} \geq 1.0 \end{cases} \tag{10}$$

$$k = \begin{cases} 1 + 0.6\bar{\lambda}n & \text{for } \bar{\lambda} < 1.0 \\ 1 + 0.6n & \text{for } \bar{\lambda} \geq 1.0 \end{cases} \tag{11}$$

The test and FE failure loads were used to assess the applicability of applying the EC3 design interaction curve to S700 high strength steel CHS beam-columns after exposure to elevated temperatures. The assessment results in Table 5 and Fig. 15 revealed that (i) the EC3 design interaction curve yields relatively conservative and scattered post-fire failure load predictions and (ii) the level of conservatism and scatter increases as θ varies from 90° to 0° (i.e. from pure compression to pure bending). This can be attributed to the inaccurate end points of the current EC3 design interaction curve, especially the bending end point for Class 3 CHS, which is limited to the elastic moment capacity without considering any benefit from the partial spread of plasticity [44].

4.5 Revised EC3 design approach

In this section, a revised EC3 design interaction curve is developed through the use of more accurate compression and bending end points. More specifically, the compression end point is now calculated based on the EC3 buckling curve 'a' with the imperfection factor α equal to 0.21, which was proposed by Zhong et al. [45] to replace the original EC3 buckling curve 'c' and shown to yield more accurate post-fire buckling resistances for S700 high strength steel CHS columns. The bending end point is now determined from Eq. (12), which is similar to Eq. (9), but with the use of the elasto-plastic section modulus W_{ep} [44] for Class 3 CHS, to account for partial plasticity in calculating cross-section bending resistances. Note that the Class 3 slenderness limit $D/(t\varepsilon^2)$ in bending is also relaxed to 140.

$$M_{Rd} = \begin{cases} W_{pl} f_y & \text{for Class 1 and 2 CHS} \\ W_{ep} f_y & \text{for Class 3 CHS} \\ W_{eff} f_y & \text{for Class 4 CHS} \end{cases} \tag{12}$$

The elasto-plastic section modulus W_{ep} is given by Eq. (13), where β_{ep} is a parameter considering a linear transition between the plastic and elastic section moduli across the Class

3 slenderness range, as defined by Eq. (14).

$$W_{ep} = W_{pl} - (W_{pl} - W_{el})\beta_{ep} \tag{13}$$

$$\beta_{ep} = \max\left(\frac{D/t - 70\varepsilon^2}{70\varepsilon^2};0\right) \quad \text{but } \beta_{ep} \leq 1.0 \tag{14}$$

The proposed design interaction curve, featuring the shape of the EC3 design interaction curve but anchored to the new compression and bending end points, was assessed for its applicability to S700 high strength steel CHS beam-columns after exposure to elevated temperatures. The assessment results, as presented in Table 5 and Fig. 16, demonstrated that the revised EC3 design interaction curve yields more accurate and consistent post-fire failure loads for S700 high strength steel CHS beam-columns than the original EC3 design interaction curve.

5. Conclusions

The structural performance and residual capacity of S700 high strength steel CHS beam-columns after exposure to elevated temperatures have been investigated, based on testing and numerical modelling. The testing programme was conducted on ten S700 high strength steel CHS beam-column specimens after exposure to various levels of elevated temperature. Upon testing, the test results were used in the numerical modelling programme to validate FE models, based on which parametric studies were carried out to generate additional numerical data over a wide range of cross-section dimensions, member lengths and loading combinations. The obtained test and numerical data were used to evaluate the applicability of the relevant room temperature design interaction curves combined with post-fire material properties for application to S700 high strength steel CHS beam-columns after exposure to elevated temperatures. On the basis of the graphical and quantitative evaluation results, the following conclusions can be drawn: (i) the design interaction curves specified in ANSI/AISC 360-16 [27] and AS 4100 [28] lead to accurate and consistent failure load predictions when applied to S700 high strength steel CHS beam-columns after exposure to elevated temperatures, and (ii) the Eurocode design interaction curve [29] results in relatively conservative and scattered predictions of failure load. A revised Eurocode design interaction curve was then proposed through employing more accurate compression and bending end points and shown to provide a higher level of design accuracy and consistency than its original counterpart.

Acknowledgements

The specimens tested in the present paper were fabricated and sponsored by SSAB, AB. The first author receives financial supports for his PhD study from a JTC Research Project (Award number: 04SBS000325C120).

References:

[1] Qiang, X., Bijlaard, F., and Kolstein, H. (2012). Dependence of mechanical properties of high strength steel S690 on elevated temperatures. Construction and Building Materials, 30, 73–79.

[2] Qiang, X., Bijlaard, F. S., and Kolstein, H. (2013). Elevated-temperature mechanical

properties of high strength structural steel S460N: Experimental study and recommendations for fire-resistance design. Fire Safety Journal, 55, 15–21.

[3] Xiong, M. X., and Liew, J. R. (2016). Mechanical properties of heat-treated high tensile structural steel at elevated temperatures. Thin-Walled Structures, 98, 169–176.

[4] Li, H. T., and Young, B. (2017). Material properties of cold-formed high strength steel at elevated temperatures. Thin-Walled Structures, 115, 289–299.

[5] Ban, H., Zhou, G., Yu, H., Shi, Y. and Liu, K. (2021). Mechanical properties and modelling of superior high-performance steel at elevated temperatures. Journal of Constructional Steel Research, 176, 106407.

[6] Xing, Y., Wang, W. and Al-azzani, H. (2021). Assessment of thermal properties of various types of high-strength steels at elevated temperatures. Fire Safety Journal, 122, 103348.

[7] Qiang, X., Bijlaard, F. S., and Kolstein, H. (2012). Post-fire mechanical properties of high strength structural steels S460 and S690. Engineering Structures, 35, 1–10.

[8] Chiew, S. P., Zhao, M. S., and Lee, C. K. (2014). Mechanical properties of heat-treated high strength steel under fire/post-fire conditions. Journal of Constructional Steel Research, 98, 12–19.

[9] Wang, W., Liu, T., and Liu, J. (2015). Experimental study on post-fire mechanical properties of high strength Q460 steel. Journal of Constructional Steel Research, 114, 100–109.

[10] Li, G. Q., Lyu, H., and Zhang, C. (2017). Post-fire mechanical properties of high strength Q690 structural steel. Journal of Constructional Steel Research, 132, 108–116.

[11] Azhari, F., Heidarpour, A., Zhao, X. L. and Hutchinson, C. R. (2017). Post-fire mechanical response of ultra-high strength (Grade 1200) steel under high temperatures: Linking thermal

stability and microstructure. Thin-Walled Structures, 119, 114–125.

[12] Azhari, F., Apon, A. A. H., Heidarpour, A., Zhao, X. L. and Hutchinson, C. R. (2018). Mechanical response of ultra-high strength (Grade 1200) steel under extreme cooling conditions. Construction and Building Materials, 175, 790–803.

[13] Su, A., Sun, Y., Liang, Y., and Zhao, O. (2020). Material properties and membrane residual stresses of S690 high strength steel welded I-sections after exposure to elevated temperatures. Thin-Walled Structures, 152, 106723.

[14] Wang, X. Q., Tao, Z. and Hassan, M. K. (2020). Post-fire behaviour of high-strength quenched and tempered steel under various heating conditions. Journal of Constructional Steel Research, 164, 105785.

[15] Zhou, X., Xue, X., Shi, Y. and Xu, J. (2021). Post-fire mechanical properties of Q620 high-strength steel with different cooling methods. Journal of Constructional Steel Research, 180, 106608.

[16] Song, L. X. and Li, G. Q. (2021). Processing and cooling effects on post-fire mechanical properties of high strength structural steels. Fire Safety Journal, 122, 103346.

[17] Zeng, X., Wu, W. B., Huo, J. S. and Elchalakani, M. (2021). Residual mechanical properties of Q890 high-strength structural steel after exposure to fire. Construction and Building Materials, 304, 124661.

[18] Wang, W., Kodur, V., Yang, X., and Li, G. (2014). Experimental study on local buckling of axially compressed steel stub columns at elevated temperatures. Thin-Walled Structures, 82, 33–45.

[19] Wang, W., Li, X. and Al-azzani, H. (2021). Experimental study on local buckling of high-

strength Q960 steel columns at elevated temperatures. Journal of Constructional Steel Research, 183, 106716.

[20] Sharhan, A., Wang, W., Li, X. and Al-azzani, H. (2021). Steady and transient state tests on local buckling of high strength Q690 steel stub columns. Thin-Walled Structures, 167, 108214.

[21] Su, A., Jiang, K., Liang, Y. and Zhao, O. (2021). Post-fire behaviour and resistances of S690 high strength steel welded I-section stub columns. Thin-Walled Structures, 169, 108422.

[22] Wang, W., Zhang, L., Ge, Y. and Xu, L. (2018). Behaviour of restrained high strength steel columns at elevated temperature. Journal of Constructional Steel Research, 148, 251–264.

[23] Wang, W., and Liu, T. (2016). Experimental and numerical study on post-fire behavior of high-strength Q460 steel columns. Advances in structural engineering, 19(12), 1873–1888.

[24] Li, G. Q., Miao, J., Song, L., Cai, W., and Jiang, J. (2020). Investigation on Postfire Residual Capacity of High-Strength Steel Columns with Axial Restraint. Journal of Structural Engineering, 146(9), 04020182.

[25] Ma, J. L., Chan, T. M. and Young, B. (2021). Cold-formed high strength steel tubular beam-columns. Engineering Structures, 230, 111618.

[26] Meng, X. and Gardner, L. (2022). Stability and design of normal and high strength steel CHS beam-columns. Engineering Structures, 251, 113361.

[27] American Institute of Steel Construction (AISC). Specification for structural steel buildings. AISC 360-16, Chicago (IL); 2016.

[28] AS 4100–1998: Reconfirmed 2016, Steel Structures. Australian Standard, Committee BD-001, 2016.

[29] EN 1993-1-12. Eurocode 3: design of steel structures - Part 1-12: additional rules for the

extension of EN 1993 up to steel grades S700. Brussels: European Committee for Standardization; 2007.

[30] Twilt, L. (1988). Strength and deformation properties of steel at elevated temperatures: some practical implications. Fire Safety Journal, 13(1), 9–15.

[31] Wang YC. Steel and composite structures - behaviour and design for fire safety. London: Spon; 2002.

[32] He, A., Sun, Y., Wu, N., and Zhao, O. (2021). Testing, simulation and design of eccentrically loaded austenitic stainless steel CHS stub columns after exposure to elevated temperatures. Thin-Walled Structures, 164, 107885.

[33] He, A., Li, H. T., Lan, X., Liang, Y., and Zhao, O. (2020). Flexural buckling behaviour and residual strengths of stainless steel CHS columns after exposure to fire. Thin-Walled Structures, 152, 106715.

[34] Cao, G., Firouzdor, V., Sridharan, K., Anderson, M. and Allen, T. R. (2012). Corrosion of austenitic alloys in high temperature supercritical carbon dioxide. Corrosion Science, 60, 246–255.

[35] Ziemniak, S. E. and Hanson, M. (2002). Corrosion behavior of 304 stainless steel in high temperature, hydrogenated water. Corrosion Science, 44(10), 2209–2230.

[36] Wang, J., and Gardner, L. (2017). Flexural buckling of hot-finished high-strength steel SHS and RHS columns. Journal of Structural Engineering, 143(6), 04017028.

[37] Meng, X., and Gardner, L. (2020). Behavior and Design of Normal-and High-Strength Steel SHS and RHS Columns. Journal of Structural Engineering, 146(11), 04020227.

[38] Cruise, R. B. and Gardner, L. (2006). Measurement and prediction of geometric

imperfections in structural stainless steel members. Structural Engineering and Mechanics, 24(1), 63–90.

[39] Zhao, O., Gardner, L., and Young, B. (2016). Testing and numerical modelling of austenitic stainless steel CHS beam–columns. Engineering Structures, 111, 263–274.

[40] Buchanan, C., Real, E., and Gardner, L. (2018). Testing, simulation and design of cold-formed stainless steel CHS columns. Thin-Walled Structures, 130, 297–312.

[41] Law, K. H., and Gardner, L. (2013). Buckling of elliptical hollow section members under combined compression and uniaxial bending. Journal of Constructional Steel Research, 86, 1–16.

[42] Karlsson Hibbitt, Inc Sorensen, ABAQUS/Standard user's Manual Volumes I-III and ABAQUS CAE Manual. Version 6.14, Pawtucket (USA) 2014.

[43] Fang, H., Chan, T. M., and Young, B. (2018). Structural performance of cold-formed high strength steel tubular columns. Engineering Structures, 177, 473–488.

[44] Meng, X., Gardner, L., Sadowski, A. J., and Rotter, J. M. (2020). Elasto-plastic behaviour and design of semi-compact circular hollow sections. Thin-Walled Structures, 148, 106486.

[45] Zhong, Y., Sun, Y., Zhao, O., and Gardner, L. Structural response and residual capacity of S700 high strength steel CHS columns after exposure to fire. Journal of Structural Engineering, Revision under review.

Table 1 Measured geometric properties and initial global geometric imperfections for S700 high strength steel CHS beam-column specimens.

Cross-section	Specimen ID	D (mm)	t (mm)	L (mm)	L_e (mm)	ω_g (mm)
CHS 139.7×10	D140-T30-E50	139.63	10.01	1501.0	1641.0	0.13
	D140-T400-E50	139.60	9.96	1501.0	1641.0	0.35
	D140-T600-E50	139.15	9.88	1501.5	1641.5	0.33
	D140-T900-E50	138.28	10.04	1523.5	1663.5	0.44
	D140-T1100-E50	139.20	9.92	1501.0	1641.0	0.23
CHS 168.3×4	D168-T30-E50	167.53	3.92	1501.0	1641.0	0.29
	D168-T400-E50	167.55	3.92	1500.0	1640.0	0.08
	D168-T600-E50	167.78	3.87	1499.0	1639.0	0.34
	D168-T900-E50	167.88	3.94	1500.0	1640.0	0.60
	D168-T1100-E50	167.50	3.88	1501.3	1641.3	0.14

Table 2 Summary of key measured post-fire material properties.

Cross-section	T (°C)	T_m (°C)	E (MPa)	f_y (MPa)	f_u (MPa)	ε_u (%)	ε_f (%)	f_u/f_y
CHS 139.7×10	30	30	203100	762.0	804.9	1.6	16.0	1.06
	400	395	210400	831.0	848.0	6.4	23.0	1.02
	600	620	213100	887.2	916.6	8.8	25.0	1.03
	900	883	216000	427.0	523.6	16.9	32.0	1.23
	1100	1095	196300	342.6	445.8	19.5	41.0	1.30
CHS 168.3×4	30	30	203200	776.5	875.1	4.6	13.0	1.13
	400	395	209400	790.0	809.2	3.6	11.0	1.02
	600	620	209800	796.7	822.6	7.9	19.0	1.03
	900	883	205300	383.4	478.9	15.2	30.0	1.25
	1100	1095	200500	252.1	364.2	15.1	30.0	1.44

Table 3 Key test results of S700 high strength steel CHS beam-columns after exposure to elevated temperatures.

Cross-section	Specimen ID	T_m (°C)	N_u (kN)	Δ_u (mm)	e_0 (mm)	$M_{u,1st,el}$ (kNm)	$M_{u,2nd,el}$ (kNm)	$M_{u,2nd,inel}$ (kNm)
CHS 139.7×10	D140-T30-E50	30	1260.0	34.13	49.10	62.03	77.20	105.03
	D140-T400-E50	395	1373.6	25.76	49.08	67.90	85.71	103.28
	D140-T600-E50	620	1313.6	24.43	49.84	65.90	82.34	97.99
	D140-T900-E50	883	695.9	16.43	50.07	35.15	39.40	46.58
	D140-T1100-E50	1095	594.6	11.54	49.36	29.49	32.68	36.35
CHS 168.3×4	D168-T30-E50	30	746.0	22.30	50.14	37.62	44.18	54.26
	D168-T400-E50	395	770.1	13.67	49.10	37.87	44.48	48.40
	D168-T600-E50	620	744.4	10.93	49.14	36.83	43.04	44.97
	D168-T900-E50	883	428.8	8.34	48.88	21.22	23.15	24.79
	D168-T1100-E50	1095	280.7	4.58	48.81	13.74	14.57	15.03

Table 4 Comparisons between test and FE failure loads.

Cross-section	Specimen ID	FE N_u/Test N_u					
		ω_g+t/100	L_e/1000 + t/100	L_e/1500 + t/100	ω_g+t/10	L_e/1000 + t/10	L_e/1500 + t/10
CHS 139.7×10	D140-T30-E50	0.992	0.980	0.985	0.981	0.969	0.973
	D140-T400-E50	0.925	0.915	0.919	0.911	0.902	0.906
	D140-T600-E50	0.998	0.988	0.992	0.984	0.973	0.978
	D140-T900-E50	1.021	1.011	1.015	1.010	0.999	1.004
	D140-T1100-E50	1.042	1.030	1.035	1.031	1.019	1.024
CHS 168.3×4	D168-T30-E50	1.013	1.012	1.013	0.974	0.971	0.973
	D168-T400-E50	0.973	0.964	0.967	0.940	0.936	0.938
	D168-T600-E50	0.997	0.994	0.997	0.964	0.956	0.960
	D168-T900-E50	0.955	0.947	0.952	0.930	0.926	0.927
	D168-T1100-E50	0.975	0.974	0.975	0.960	0.954	0.958
	Mean	0.989	0.982	0.985	0.969	0.961	0.964
	COV	0.034	0.035	0.034	0.037	0.036	0.036

Table 5 Comparisons of test and FE failure loads with predicted failure loads.

T (°C)	$N_u/N_{u,pred}$							
	AISC		AS		EC3		Revised EC3	
	Mean	COV	Mean	COV	Mean	COV	Mean	COV
30	1.06	0.08	1.12	0.09	1.20	0.11	1.07	0.11
400	1.03	0.05	1.10	0.07	1.17	0.09	1.04	0.08
600	1.03	0.05	1.10	0.07	1.16	0.09	1.04	0.08
900	1.05	0.05	1.11	0.05	1.17	0.07	1.05	0.04
1100	1.02	0.06	1.08	0.06	1.14	0.08	1.02	0.06
Total	1.04	0.06	1.10	0.07	1.17	0.09	1.04	0.08

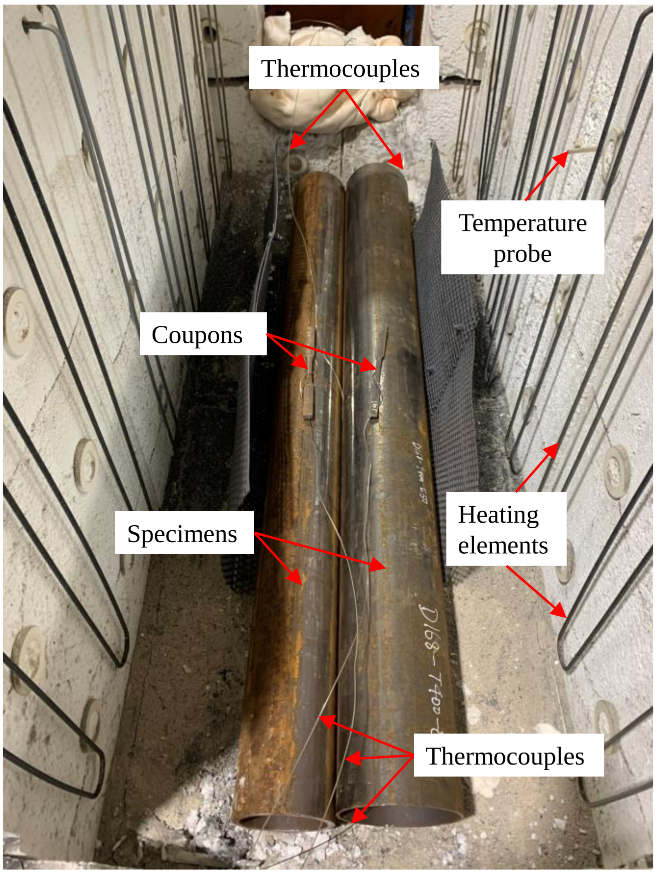

Fig. 1. Electric furnace.

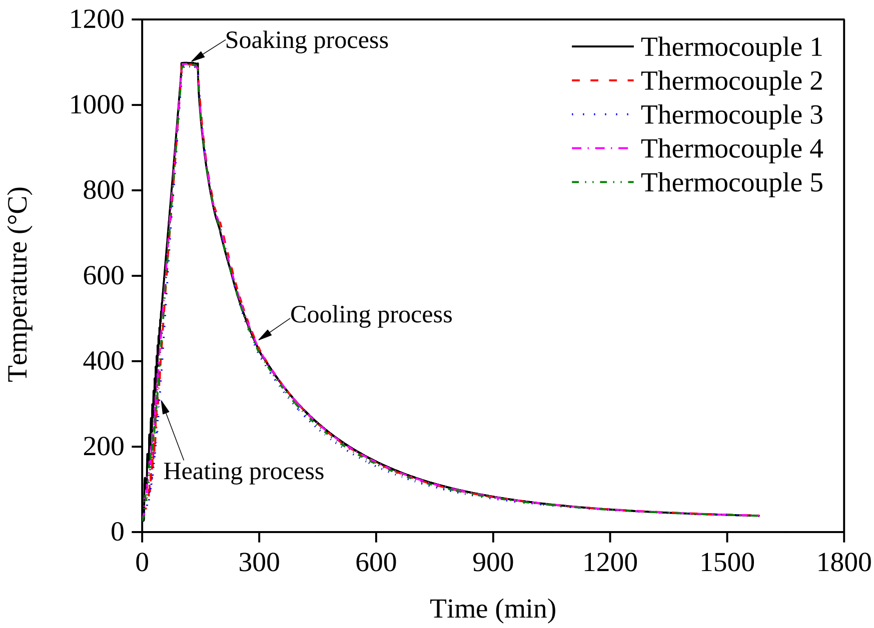

Fig. 2. Temperature–time curves for a typical set of specimens heated up to 1100 °C and cooled down.

Fig. 3. Surface colours of S700 high strength steel after exposure to various levels of elevated temperature.

Fig. 4. Material tensile coupon test setup.

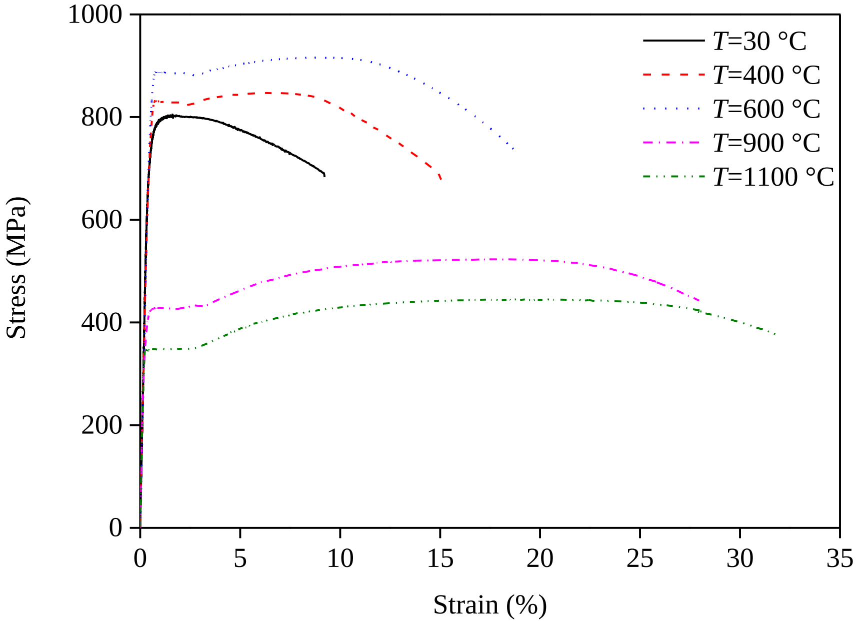

(a) CHS 139.7×10

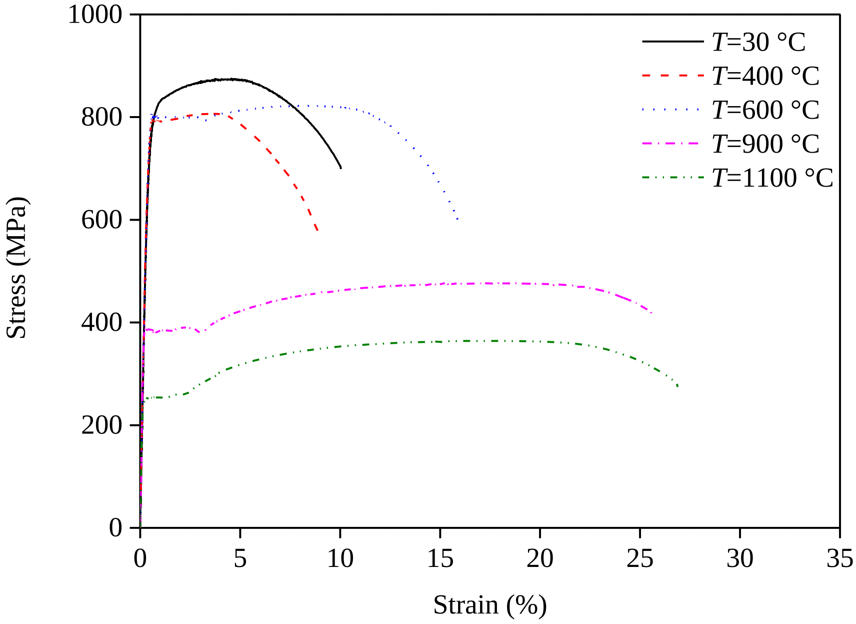

(b) CHS 168.3×4

Fig. 5. Measured post-fire stress–strain curves.

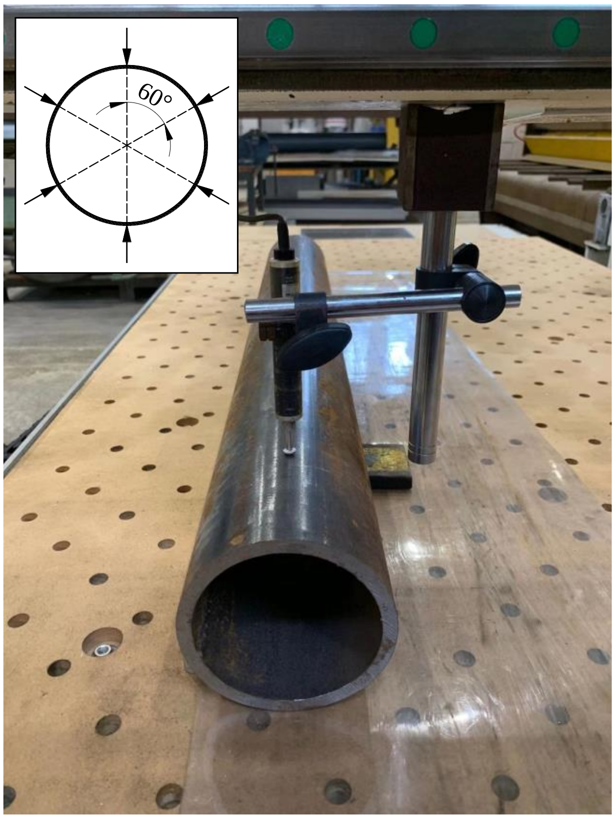

Fig. 6. Test setup for initial global geometric imperfection measurements.

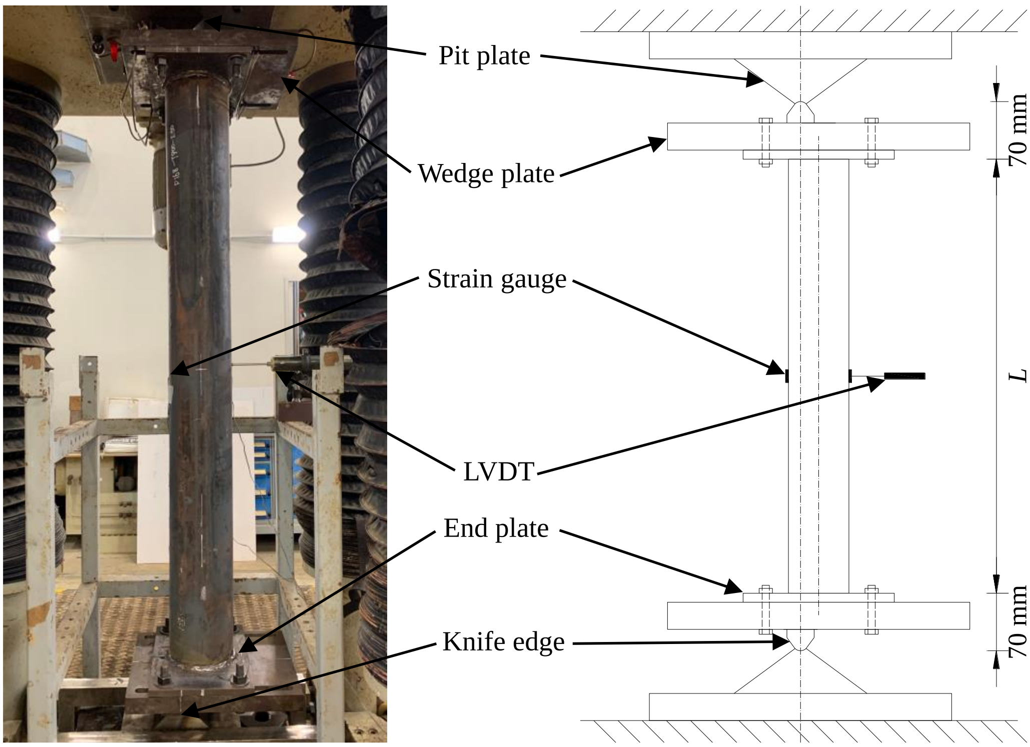

(a) Photograph

(b) Schematic diagram

Fig. 7. Beam-column test setup.

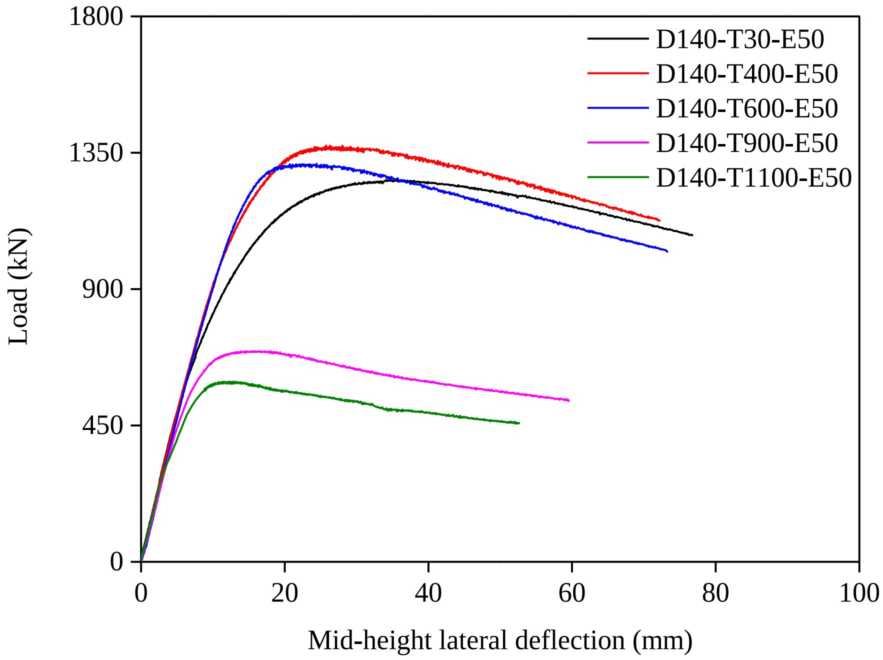

(a) CHS 139.7×10

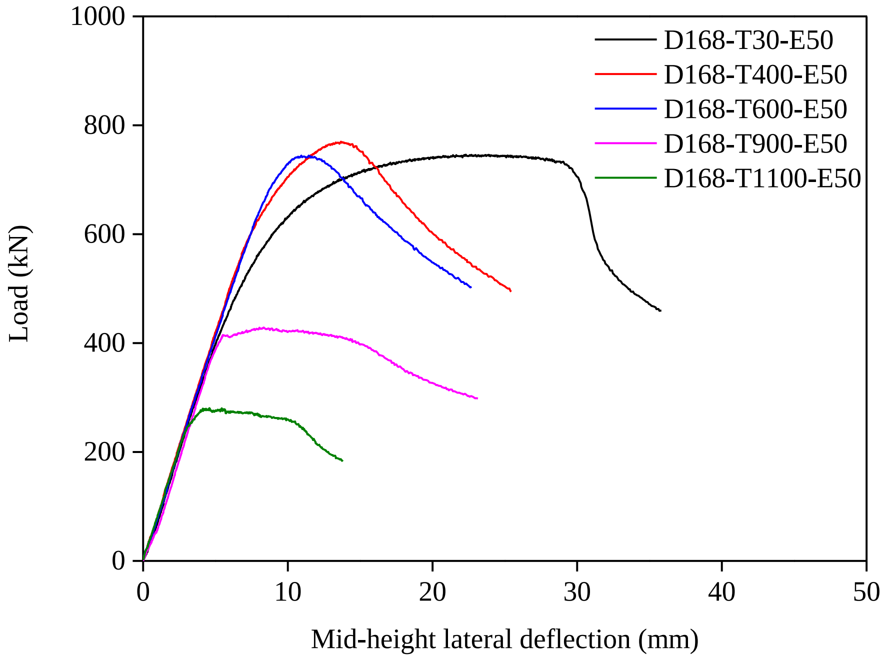

(b) CHS 168.3×4

Fig. 8. Load–mid-height lateral deflection curves for S700 high strength steel CHS beam-column specimens after exposure to elevated temperatures.

(a) CHS 139.7×10

(From left to right: D140-T30-E50, D140-T400-E50, D140-T600-E50, D140-T900-E50, D140-T1100-E50)

(b) CHS 168.3×4

(From left to right: D168-T30-E50, D168-T400-E50, D168-T600-E50, D168-T900-E50, D168-T1100-E50)

Fig. 9. Failure modes of S700 high strength steel CHS beam-column specimens upon testing.

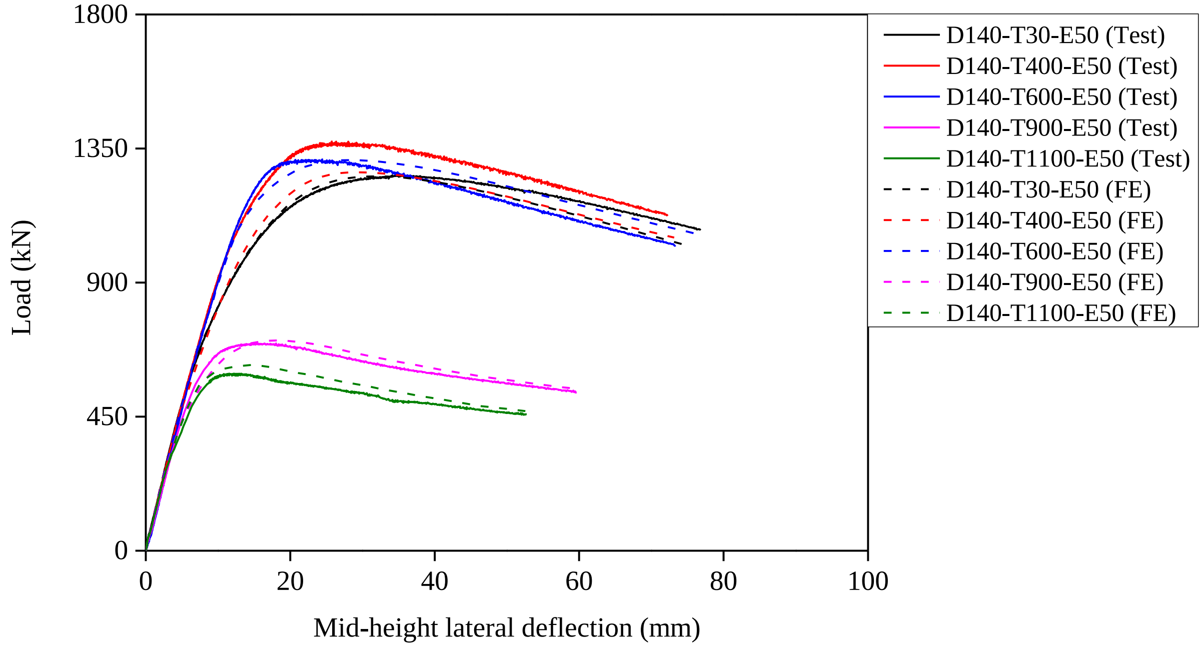

(a) CHS 139.7×10

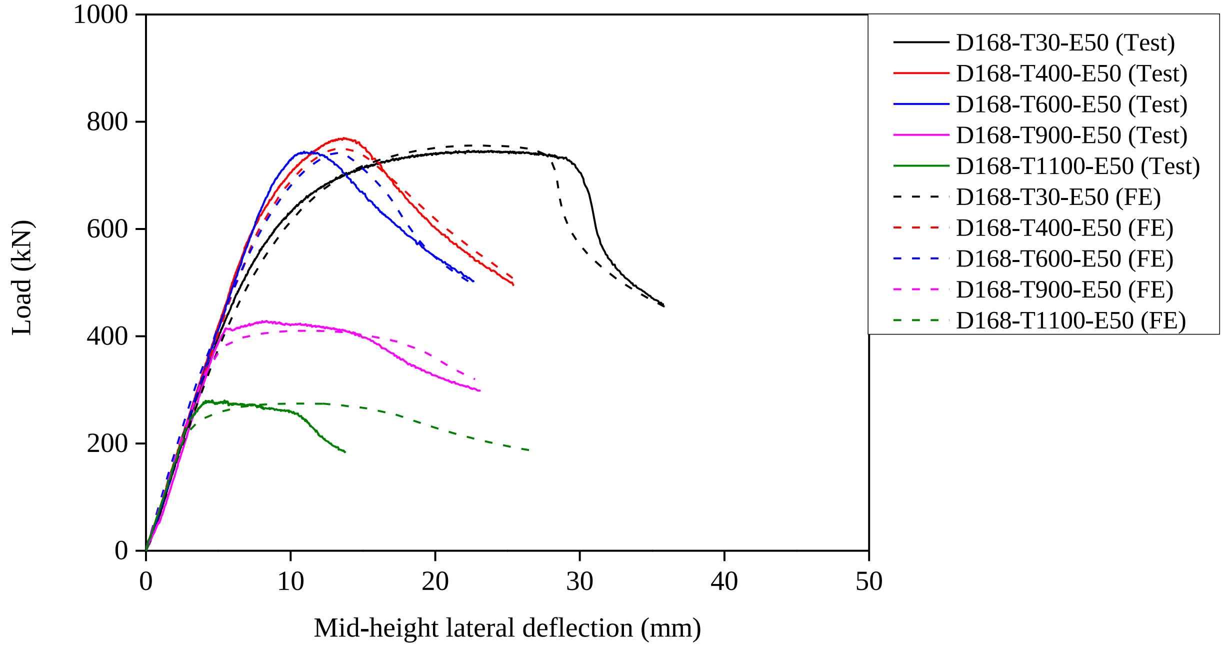

(b) CHS 168.3×4

Fig. 10. Test and FE load–mid-height lateral deflection curves.

(a) D140-T600-E50

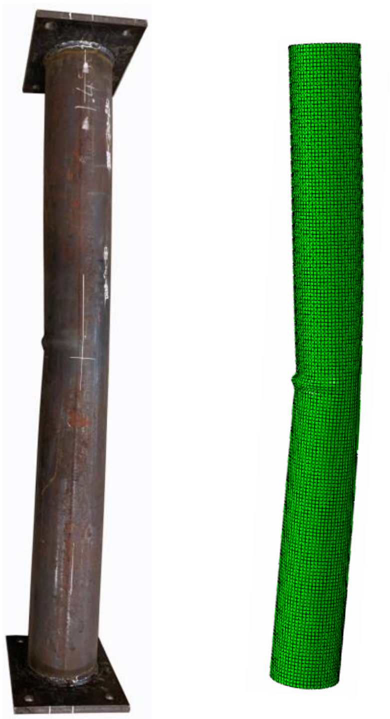

(b) D168-T600-E50

Fig. 11. Test and FE failure modes for typical specimens.

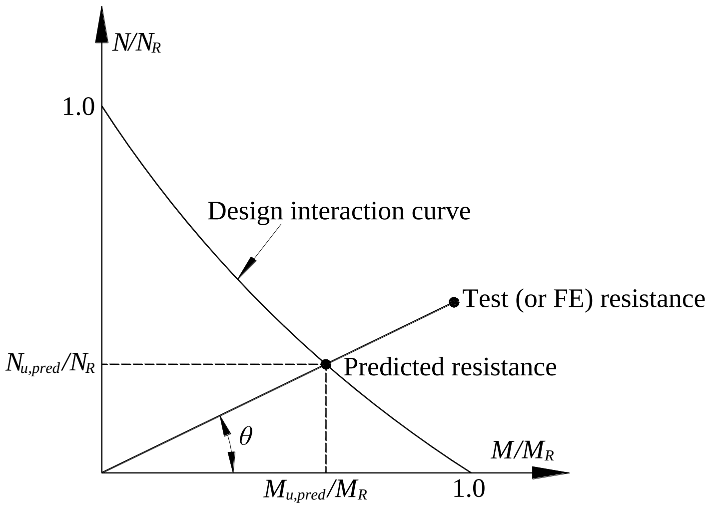

Fig. 12. Definition of θ on axial load–moment interaction curve.

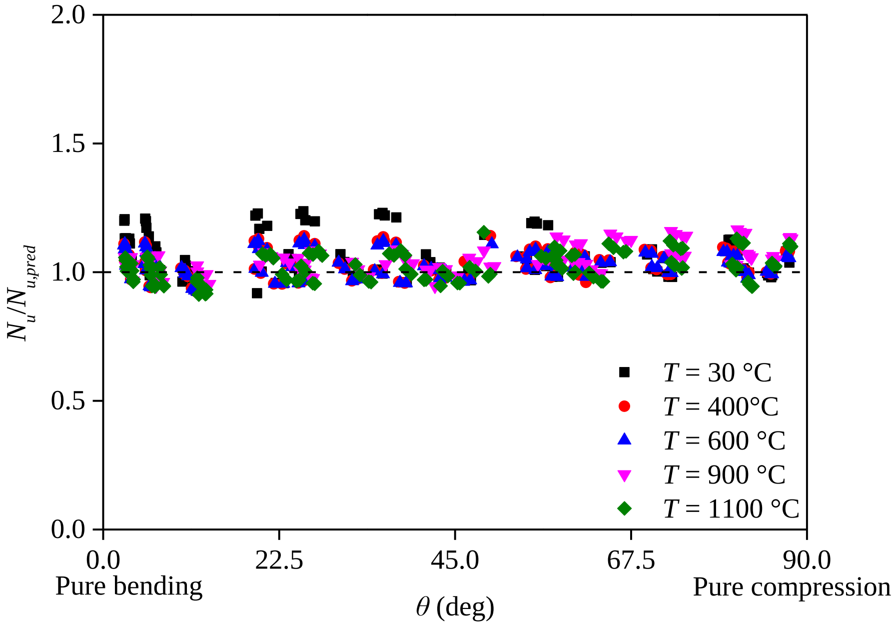

Fig. 13. Comparisons of test and FE failure loads with AISC failure load predictions.

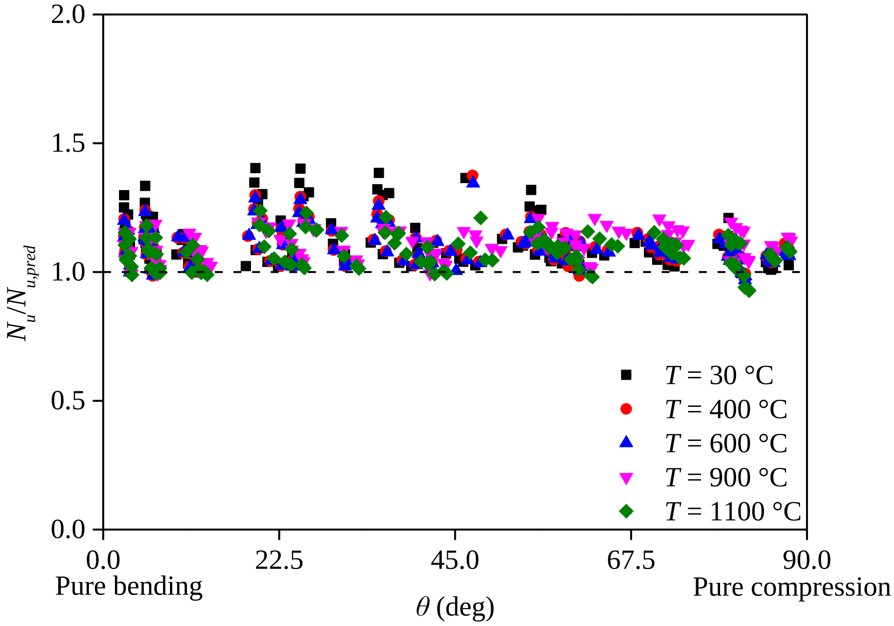

Fig. 14. Comparisons of test and FE failure loads with AS failure load predictions.

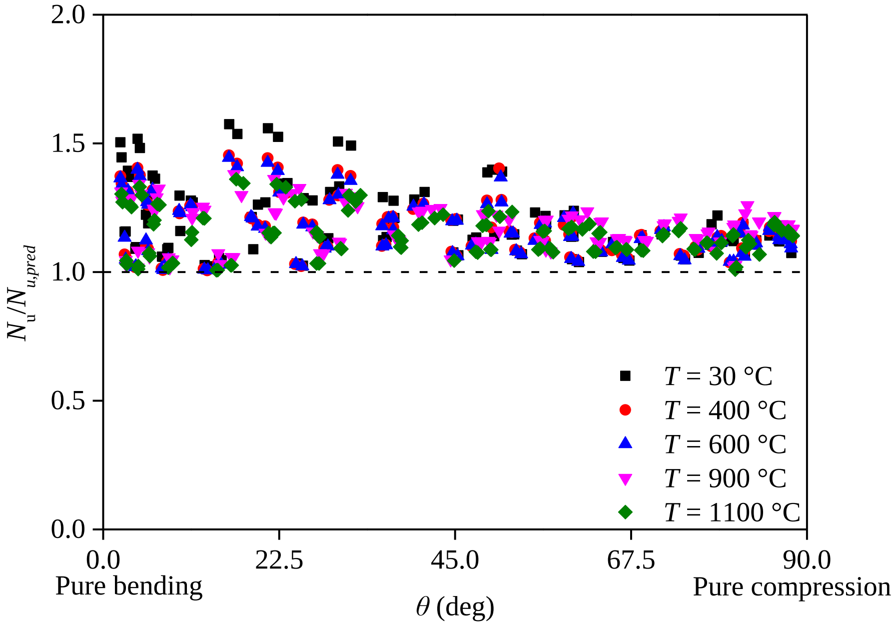

Fig. 15. Comparisons of test and FE failure loads with EC3 failure load predictions.

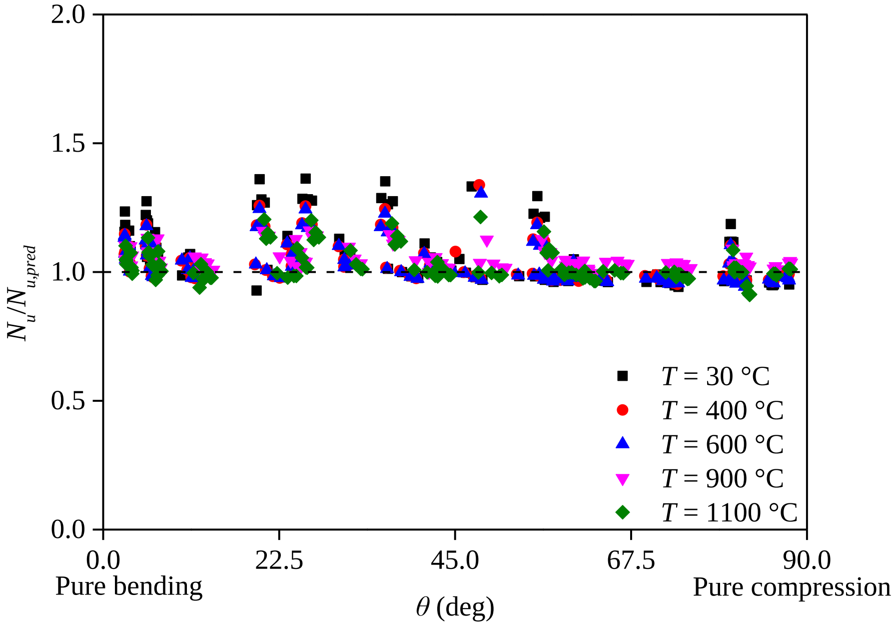

Fig. 16. Comparisons of test and FE failure loads with failure load predictions from revised EC3 design approach.